Rapid Route to Efficient, Scalable, and Robust Perovskite Photovoltaics in Air

Authors: Florian Hilt[1], Michael Q. Hovish[1], Nicholas Rolston[2], Karsten Brüning[3], Christopher J. Tassone[3], Reinhold H. Dauskardt[1*]

Affiliations:

[1]Department of Materials Science and Engineering, Stanford University, Stanford, CA 94305, USA

[2]Department of Applied Physics, Stanford University, Stanford, CA 94305, USA

[3]Stanford Synchrotron Radiation Lightsource (SSRL), SLAC National Accelerator Laboratory, Menlo Park, CA 94025, USA

*Correspondence to: rhd@stanford.edu

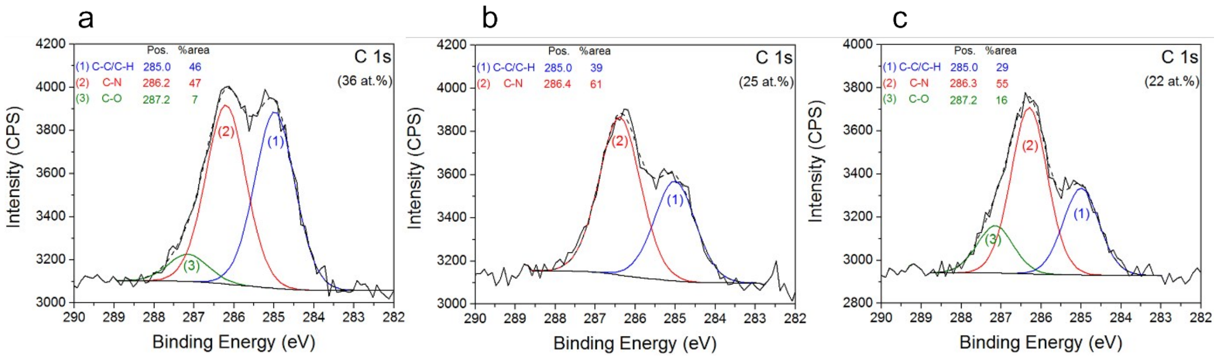

Figure S1. XPS curve-fitting of carbon. **a**, Spin-coated, **b**, RSPP and **c**, Hot air-cured films. Alkoxy groups for spin-coated and hot-air cured films are noted but no carboxyl moieties have been detected, meaning no residual acetate groups are present in the layers. In both cases, oxidized hydrocarbons were present only at the top surface of the films. Additionally, aliphatic (C-C bond) and amine (C-N) functional groups were detected for all the films.

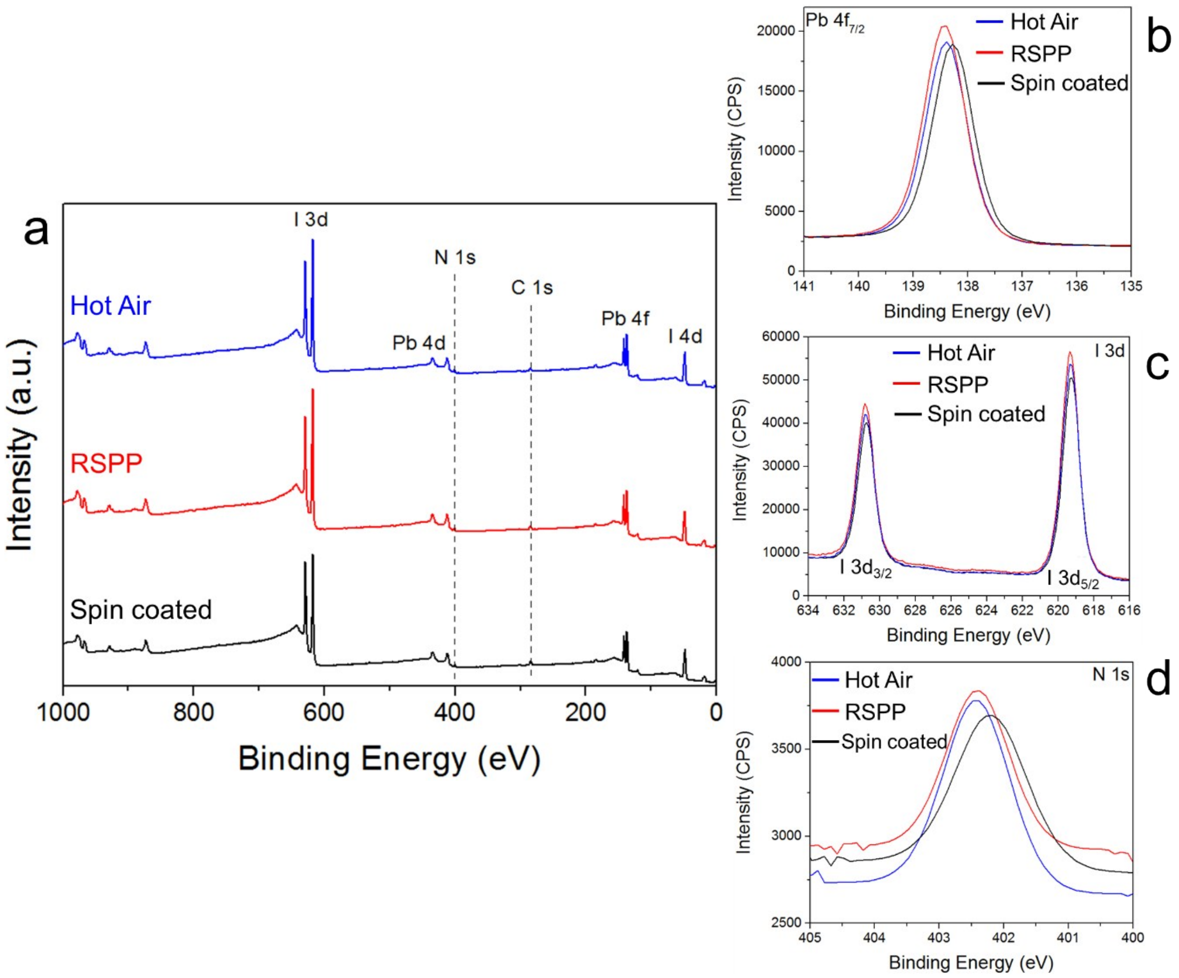

Figure S2. Thin films compositions. a, X-ray photoelectron spectroscopy survey spectrum. Curve-fitting of **b**, Pb $4f_{7/2}$, **c**, I 3d, and **d**, N 1s core-level for spin coated, RSPP and hot gas-cured. The experimental signals of Pb $4f_{7/2}$ at 138.4 eV (± 0.5 eV) and of I $3d_{5/2}$ and $3d_{3/2}$ at 619.3 eV (± 0.05 eV) and 630.8 eV (± 0.05 eV), respectively, are consistent with the presence of Pb^{2+} in PbI_3^- and PbI_2. No metallic lead was present in the films. The spectral contribution of nitrogen is similar for all the conditions used and is typical of a $MAPbI_3$ structure. The contribution centered around 402.4 eV (± 0.05 eV) was attributed to N-C in $CH_3NH_3^{+2}$. No contribution of methylamine (CH_3NH_2, *ca.* 401 eV) was noted, suggesting that the perovskite films have not aged significantly, even in the open air.

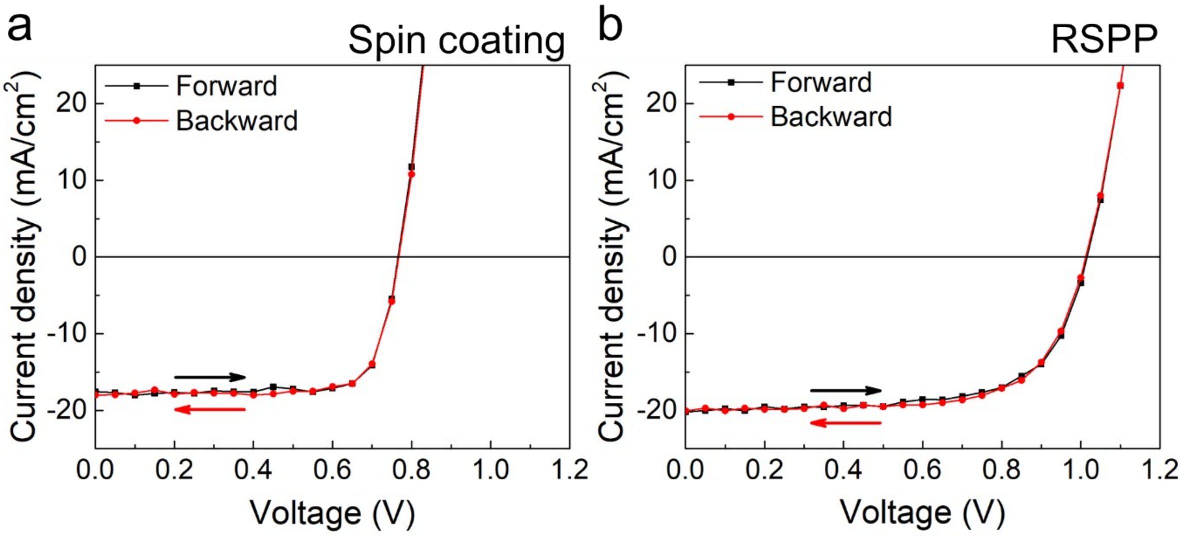

Figure S3. Current density/voltage plots in both forward (black) and backward (red) direction. a, Representative of the control device and **b**, Representative of the RSPP device, showing minimal hysteresis in both cases.

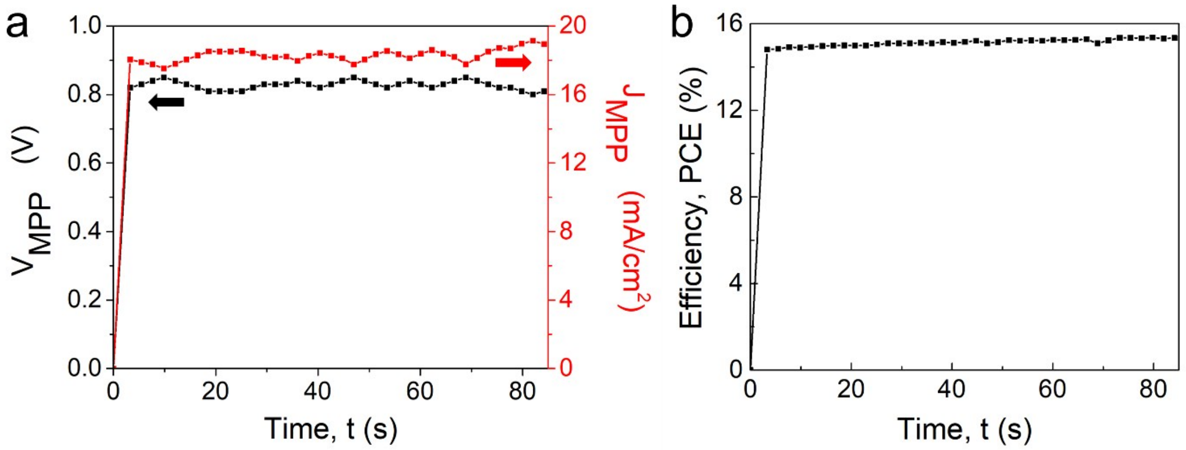

Figure S4. Stabilization of *J-V* curve parameters representative of the RSPP device. a, Stabilization of photocurrent density and voltage at maximum power point. **b**, Maximum power point data tracked in function of time.

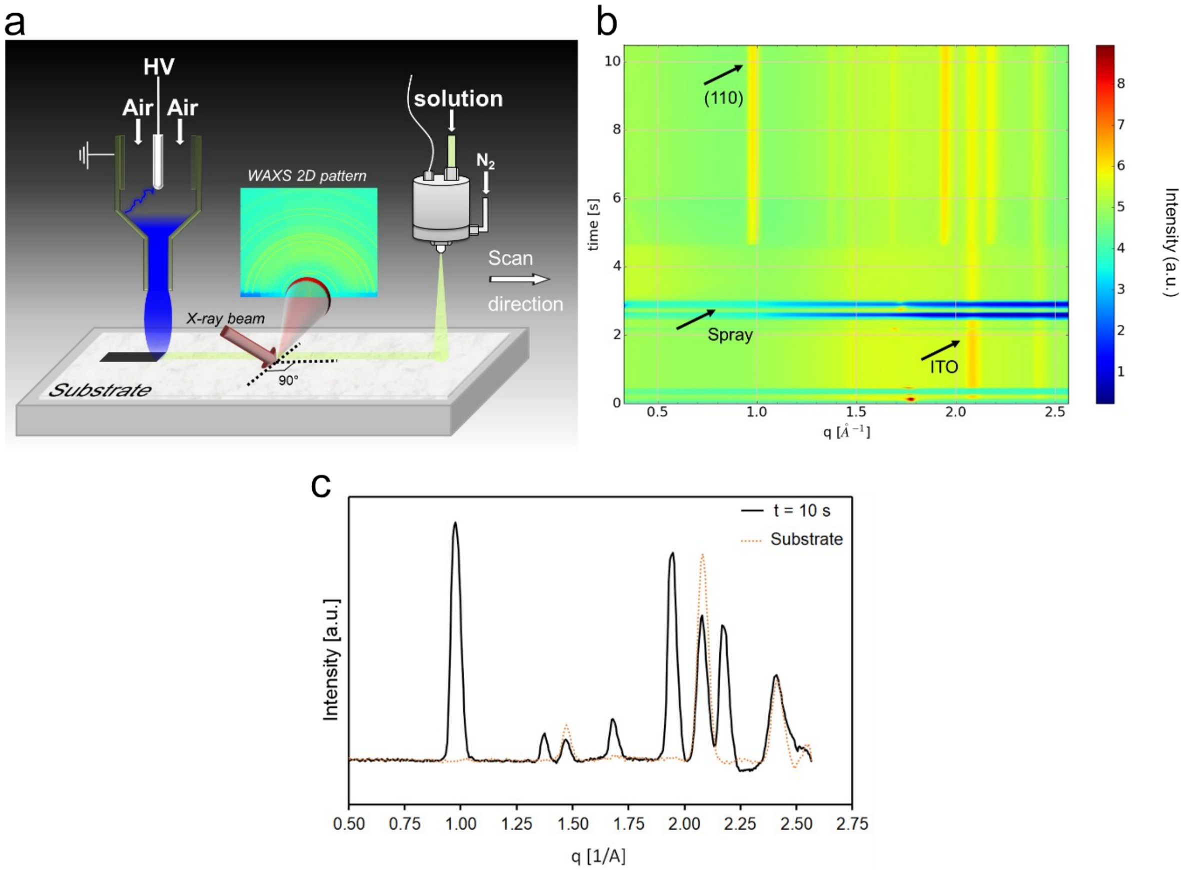

Figure S5. Wide angle X-ray scattering measurements. **a**, RSPP system integrated into the beamline representing the x-ray beam orthogonal to the scan direction. **b**, Contour plot of the WAXS data as a function of time. **c**, Integrated diffraction curves of the perovskite at t = 10s regarding Fig. 1d, which represents the perovskite crystal after spray-plasma deposition.

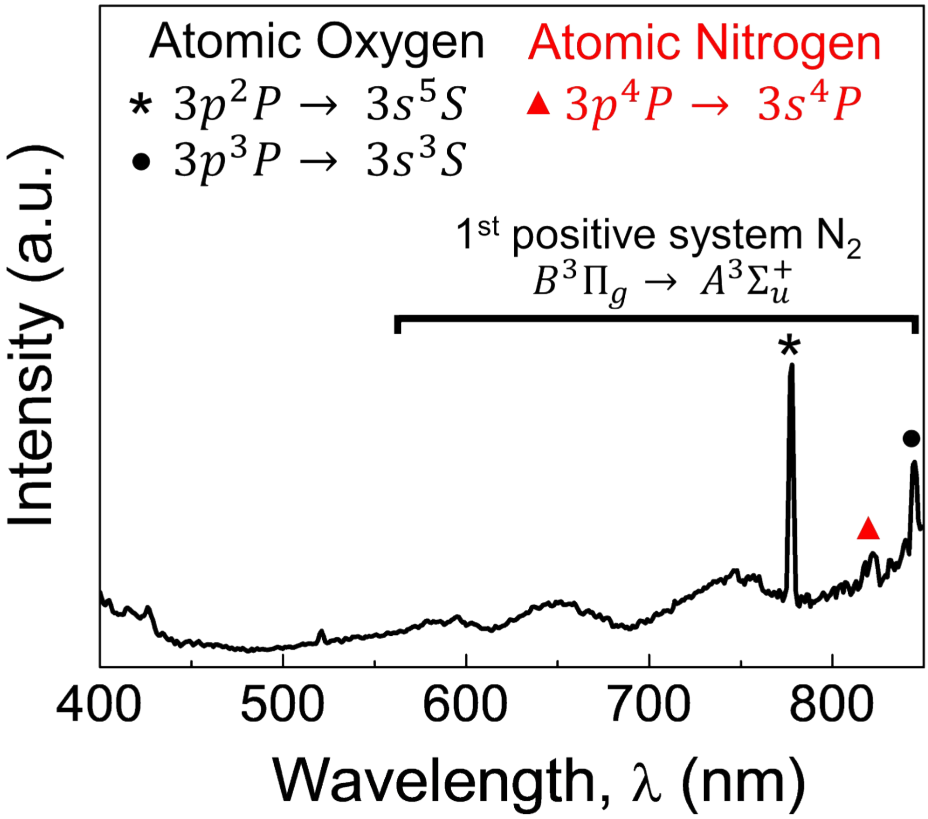

Figure S6. Optical emission spectroscopy spectrum for atmospheric pressure air plasma post-discharge in the visible range.

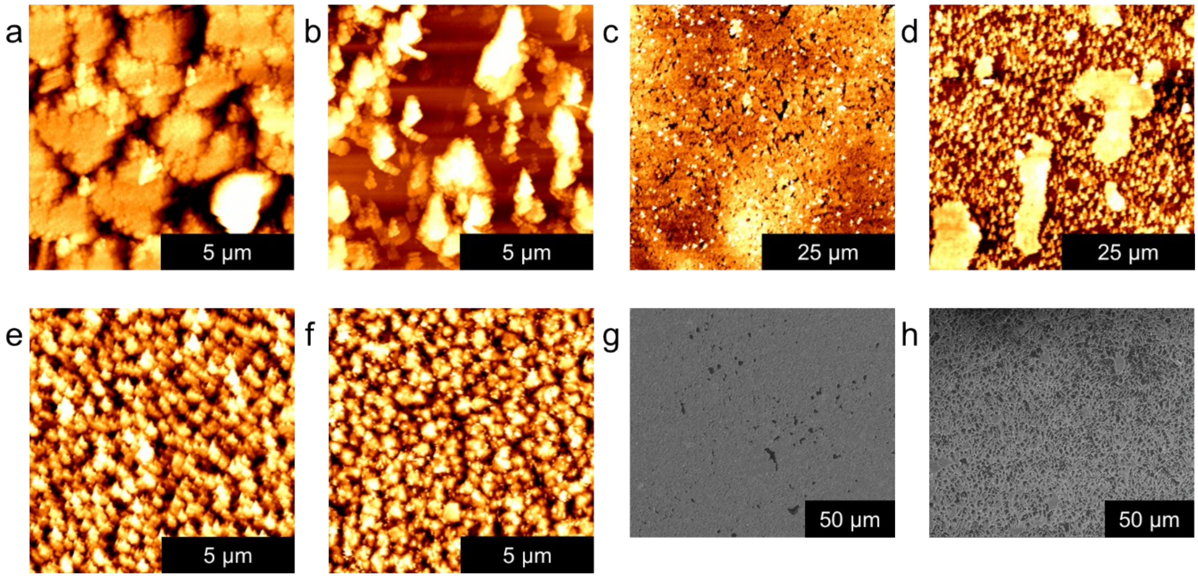

Figure S7. Microscopy of fractured perovskite films. a-b, 10 x 10 um AFM scan on fractured RSPP surface, **c-d**, 50 x 50 um AFM scan on fractured RSPP surface, **e-f**, 10 x 10 um AFM scan on fractured spin coated perovskite surface and **g-h**, SEM scan on fractured RSPP surface.

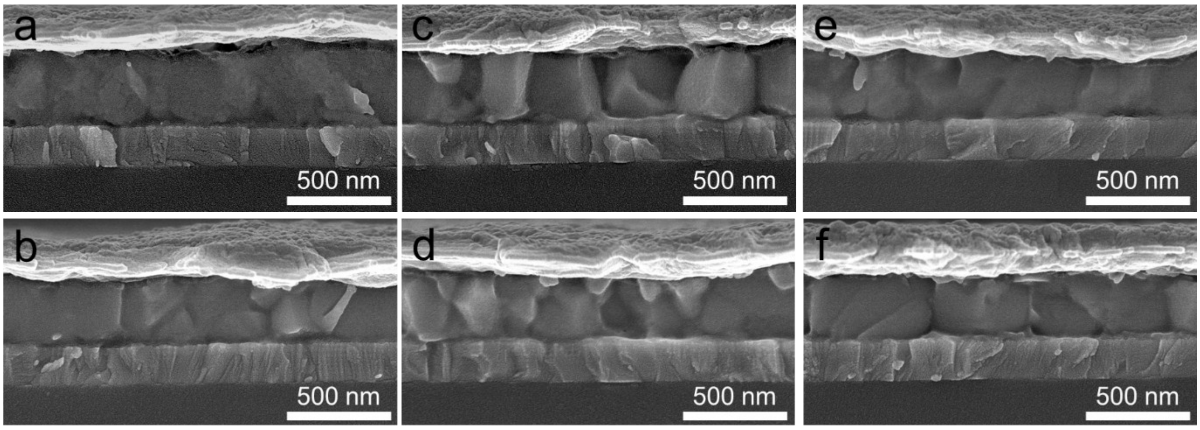

Figure S8. Large-scale RSPP of uniform $MAPbI_3$ layers. Representative of the devices that performed **a**, The highest J_{SC}, and **b**, The lowest J_{SC}. **c**, The highest V_{OC} and FF, and **d**, The lowest V_{OC}. **e**, The lowest FF. **f**, Representative of the best-performing spin-coated device (PCE = 15.4%).

Table S1. Relative atomic concentration of carbon, nitrogen, oxygen, lead and iodine, and I/Pb ratio. The gas temperature obtained at a scan speed of 40 mm/s and a nozzle-to-substrate height of *a*=40mm is also indicated. The observed I/Pb ratio values are low considering the ideal stoichiometric value of 3.0, but are still within the tolerant region. This sub-stoichiometry arises from the presence of PbI_2 in the films.

	Elemental composition (at.%)				I/Pb ratio	Gas temperature (°C)
	C	N	Pb	I		
Ideal $MAPbI_3$ perovskite	16.67	16.67	16.67	50	3.0	-
Spin coated	37	11	14	38	2.7	-
RSPP	25	12	17	46	2.7	152 ± 4
Hot air	22	11	18	49	2.7	155 ± 5

Table S2. Solar cell devices performance parameters. The average and standard deviation values of a batch of 25 identically processed solar cell devices are shown.

		Current density (mA·cm^{-2})	Open-circuit voltage (V)	Fill factor	Efficiency (%)
Spin coated	Best-performing cell	22.4	0.98	0.70	15.4
	Average ± standard deviation	21.7 ± 0.6	0.93 ± 0.03	0.70 ± 0.02	14.2 ± 0.6
RSPP	Best-performing cell	21.8	1.05	0.69	15.7
	Average ± standard deviation	20.7 ± 1.9	0.97 ± 0.03	0.62 ± 0.04	12.6 ± 1.8

Equation S1. Open-circuit voltage.

$$V_{OC} = \frac{k_B T}{q} \ln\left(\frac{J_{SC}}{J_0} + 1\right)$$

k_B, Boltzmann constant.

T, temperature.

q, charge.

J_{SC}, short-circuit current density.

J_0, saturation current density.

Equation S2. Dark current.

$$J_0 \sim \frac{qD}{L_{diff}}$$

q, charge.

D, carrier diffusivity.

L_{diff}, diffusion length.

Equation S3. Rayleigh number. Thermal energy is transferred to the precursor-solvate through convection with the background gas.

$$R_A = \frac{(g\Delta\rho L^3)}{\alpha\mu} \approx 10^6$$

g, acceleration due to gravity.
ρ, volumetric mass.
L, characteristic length scale.
α, thermal diffusivity.
μ, dynamic viscosity.

Equation S4. Thermal radiation heat transfer.

$$Q = \sigma \cdot A \cdot \left(T_{plasma}^{4} - T_{solvent}^{4}\right) = 24.8\ mJ$$

σ, Stefan-Boltzmann Constant.

A, area

T, temperature.

Equation S5. Temperature increase occurring from thermal radiation heat transfer. The background gas primarily transfers heat to the system via convection.

$$\Delta T = \frac{Q}{(m \cdot C)} \approx 0.1K$$

Q, heat.
m, mass.
C, heat capacity.

Equation S6. Free energy of a growing particle (homogeneous nucleation).

$$\Delta G = 4\pi R^2 \gamma - \frac{4\pi}{3} R^3 g_v$$

R, radius of the growing particle.

γ, surface energy of the growing particle.

g_v, free energy associated with the bulk volume.

Equation S7. Energy barrier to nucleation.

$$\Delta G^* = \frac{4}{27} \frac{\left(\sum_i \eta_i \Gamma_i\right)^3}{(\mu_2 - \mu_1)^2} = \frac{16\pi\gamma^3}{3 \ g_v^2}$$

γ, surface energy of the growing particle.

g_v, free energy associated with the bulk volume.

Equation S8. Capacitance. We consider a steady-state situation (d/dt = 0) and a fixed particle radius. The perovskite particle is assumed to be an isolated conducting sphere.

$$C_0 = 4\pi\varepsilon_0\varepsilon_r R$$

ε_0, permittivity of free space.

ε_r, relative permittivity of the solvent surrounding the perovskite particle.

R, particle radius.

Equation S9. Avrami equation.

$$dV_{\beta}^{e} \sim G^{n} t^{n} dt \quad (1)$$

with the extended volume of the crystalline phase V_{β}^{e} and the Avrami exponent n.

$$\frac{1}{1-Y} dV_{\beta} \sim dV_{\beta}^{e} \quad (2)$$

with $Y = \frac{V_{\beta}}{V}$ being the volume fraction of the perovskite crystallites, proportional to the integrated area under the dominant perovskite diffraction peak at q = 1.0 Å^{-1}.

From integration follows:

$$\frac{dV_{\beta}^{e}}{dt} = \frac{1}{1-Y} \frac{dY}{dt} = G^{n} t^{n} \quad (3)$$

We thus obtain G^{n} from the experimental data as:

$$G^{n} \sim \frac{1}{t^{n}} \frac{1}{1-Y} \frac{dY}{dt} \quad (4)$$

$$T(t) = at + b \quad (5)$$

with the parameters: a = 385.4 K and b = -10.6 K/s.